

# A prototype for convective margin shifts

B. R. Lintner and J. D. Neelin

Department of Atmospheric and Oceanic Sciences and Institute of  
Geophysics and Planetary Physics, University of California at Los Angeles  
Los Angeles, California, USA

---

B. R. Lintner and J. D. Neelin, Department of Atmospheric and Oceanic Sciences, and Institute  
of Geophysics and Planetary Physics, University of California at Los Angeles, Los Angeles, CA  
90095-1565, USA (ben@atmos.ucla.edu; neelin@atmos.ucla.edu)

1 Regional precipitation anomalies under El Niño or global warming scenar-  
2 ios manifest considerable spatial variability, especially in the vicinity of trop-  
3 ical deep convective zones. Using a simplified set of equations, we develop  
4 an analytic prototype of convective margins for tropical land regions sub-  
5 ject to inflow from adjacent ocean regions. The approach yields an expres-  
6 sion for the location of the convective margin from which it is straightfor-  
7 ward to deduce how climate perturbations impact the margin. We compare  
8 the results of the prototype to full model simulations of the equatorial South  
9 American precipitation response to El Niño forcing and find general agree-  
10 ment. Analysis of the observations supports the convective inflow margin pro-  
11 totype's applicability to appropriately simple basic state configurations.

## 1. Introduction

12 The gross-scale climate signatures of El Niño outside of the Pacific (the “remote tele-  
13 connection”) include tropospheric and surface warming and widespread deficits in rainfall  
14 [*Ropelewski and Halpert, 1987; Wallace et al., 1998*]. While many studies have explored  
15 the mechanisms underlying these gross-scale responses [e.g., *Klein et al., 1999; Saravanan*  
16 *and Chang, 2000; Chiang and Sobel, 2002; Su and Neelin, 2002; Chiang and Lintner,*  
17 *2005; Lintner and Chiang, 2005; Neelin and Su, 2005*], the regional scale features of the  
18 teleconnection are less well understood. For example, observed El Niño-related tropi-  
19 cal precipitation anomalies exhibit a highly nontrivial spatial structure, with significant  
20 regional differences in the magnitudes and even sign of the anomalies [*Dai and Wigley,*  
21 *2000*].

22 The complex regional behavior points to the influence of multiple mechanisms on tropi-  
23 cal precipitation variability [*Neelin and Su, 2005*]. For example, *Neelin et al.* [2003]  
24 and *Chou and Neelin* [2004] proposed a set of two related mechanisms—“upped-ante” and  
25 “rich-get-richer”—that are conceptually useful in the interpretation of the spatial structure  
26 of precipitation anomalies under El Niño or global warming forcing. Briefly, upped-ante  
27 postulates preferential moistening of convective zones relative to nonconvecting zones  
28 as warming increases the moisture threshold necessary to sustain convection, while the  
29 rich-get-richer mechanism suggests that the anomalous convective-nonconvective moisture  
30 gradient enhances convective region moisture convergence. While these mechanisms pro-  
31 vide a template for precipitation anomaly spatial structures—i.e., moistening of convective  
32 centers and drying along convective margins—their manifestation depends sensitively on

33 factors such as the intensity and location of climatological convection and the relationship  
34 between winds and moisture gradients.

35 From a modeling perspective, complexities in the spatial characteristics of tropical pre-  
36 cipitation variability pose additional challenges. Simulations of El Niño show large inter-  
37 model discrepancies in the distribution and amplitude of precipitation changes [*Joseph*  
38 *and Nigam, 2005*]. Considerable intermodel disagreement is also evident in global warm-  
39 ing simulations of precipitation, especially near strongly convecting regions in the trop-  
40 ics [*Neelin et al., 2006*]. Understanding why different models simulate the precipitation  
41 changes that they do is thus crucial to the use of models as predictive or interpretative  
42 tools.

43 Our principal interest here is to understand the behavior of the tropical convective mar-  
44 gin, i.e., the boundary separating convecting and nonconvecting regions, for the specific  
45 case of land region moisture inflow from a neighboring ocean region. We develop a pro-  
46 totype for the position of inflow margins and how margin locations vary under climate  
47 perturbations. Given the large discrepancies between models, the simplicity of the solu-  
48 tion presented here is useful for developing intuition about a particular set of interactions  
49 contributing to precipitation anomalies under climate change scenarios.

## 2. Model of the convective margin

### 2.1. Simplification of the thermodynamic equations

50 We start from vertically-averaged temperature and moisture equations, as in [*Neelin and*  
51 *Zeng, 2000*, see also the supplementary material], and apply them, in steady-state and 1D,  
52 to a semi-infinite land region lying to the west of an ocean region (Figure 1). We assume

53 evaporation to be small and therefore ignore it in the moisture equation. Precipitation  
54 is modeled as  $P = \tau_c^{-1}(q - q_c(T))$ , where  $q$  is vertically-averaged moisture,  $q_c(T)$  is a  
55 vertically-averaged quasi-equilibrium (QE) value of moisture as a function of vertically-  
56 averaged tropospheric temperature,  $T$ , and  $\tau_c$  is a convective-adjustment timescale. For  
57  $q < q_c(T)$ ,  $P = 0$ .

58 Given these assumptions, the land region thermodynamic equations become:

$$M_s \nabla \cdot \mathbf{v} = P + F_T \quad (1)$$

$$-(M_{qp}q) \nabla \cdot \mathbf{v} = -u_q \partial_x q - P \quad (2)$$

59 where  $F_T$  is the total flux forcing of the atmosphere,  $u_q$  is the projection of the zonal  
60 windfield onto the vertical structure of moisture, and  $M_s$  and  $M_q$  are dry static stability  
61 and moisture stratification, respectively. Since the net surface flux vanishes in equilibrium,  
62  $F_T$  is just the net top-of-the atmosphere radiative forcing. We take  $F_T > 0$ , which is  
63 appropriate for tropical or summertime continents [*Chou and Neelin, 2003*].  $M_s$  is assumed  
64 to be a spatial constant, though with distinct values in the convecting and nonconvecting  
65 regions, while  $M_q$  is expressed as  $M_{qp}q$ . Note that for  $T$  and  $q$  in temperature units (e.g.,  
66 K),  $P$  and  $F_T$  are in units of  $\text{K s}^{-1}$ ;  $M_s$  and  $M_q$  are also in K.

67 An additional approximation, that of weak temperature gradients (WTG), has been  
68 utilized in (1) [*Bretherton and Sobel, 2002; Sobel et al., 2002*]. WTG follows from the ob-  
69 served tendency for gradients in  $T$  to be small within the Tropics, as a result of the efficient  
70 lateral homogenization of temperature by equatorial wave dynamics. As such, advective  
71  $T$  gradients in (1) are neglected, as are any temperature-related spatial dependences of

72 the flux terms. The utility of WTG is that, for specified  $T$ ,  $\nabla \cdot \mathbf{v}$  is determined by (1)  
 73 and can be substituted into (2). Ocean region  $q$  is assumed given, with  $q_0$  representing  
 74 the boundary value for land region moisture.

## 2.2. Solution for the nonconvecting region

75 Integrating (2) westward from the boundary (at  $x = 0$ ) for the case of  $u_q = \text{constant}$   
 76 yields  $q(x) = q_0 e^{-\lambda x}$ , for all  $x$  such that  $q < q_c(T)$ , where the length-scale  $\lambda^{-1}$  is given  
 77 by  $-u_q M_s (M_{qp} F_T)^{-1}$ . The position of the convective margin relative to the land-ocean  
 78 interface,  $x_c$ , is then given by the value of  $x$  for which  $q = q_c(T)$ , i.e.,:

$$x_c = -\lambda^{-1} \ln(q_c(T)/q_0) \quad (3)$$

## 2.3. Solution for the convecting region

79 Within the convecting region (i.e.,  $x \leq x_c$ ), QE constrains  $q$  to be close to  $q_c(T)$ ,  
 80 so  $M_q \approx M_{qp} q_c(T)$ . Eliminating  $\nabla \cdot \mathbf{v}$  between equations (1) and (2) and using the  
 81 definition of  $P$  leads to a first order differential equation with solution  $q(x) = q_c(T) +$   
 82  $\tau_c M_{qp} q_c(T) F_T M^{-1} (1 - e^{\lambda_c(x-x_c)})$ , where the gross moist stability  $M = M_s - M_q$  [Yu *et al.*,  
 83 1998] is approximately constant.  $\lambda_c^{-1} = -u_q \tau_c M_s M^{-1}$  defines a characteristic length-scale  
 84 over which  $q$  transitions to its maximum value. The precipitation field is thus:

$$P(x) = \frac{M_{qp} q_c(T)}{M} F_T (1 - e^{\lambda_c(x-x_c)}) \quad (4)$$

85 In the “strict-QE limit” of  $\tau_c \rightarrow 0$ ,  $P = M_{qp} q_c(T) F_T M^{-1}$ , i.e., the precipitation field  
 86 transitions abruptly from 0 to its peak value at the margin  $x_c$ .

## 2.4. Perturbations of the convective margin

87 Our primary interest in developing the convective margin model is to understand what  
88 happens to the convective margin under anomalous climate forcing (e.g., El Niño or global  
89 warming). Consider a  $T$  increase  $\delta T$ . According to (3), the location of the margin  $x_c$   
90 recedes from the coastline, since  $q_c(T)$  increases. Precisely how far the margin moves de-  
91 pends on how far the inflow value of moisture  $q_0$  is from the threshold for deep convection,  
92 the (low-level) wind, and the thermodynamic dependences of  $\lambda^{-1}$ .

93 What happens to the precipitation field in the warming scenario? Consider an anoma-  
94 lous marginal displacement  $\delta x_c$  associated with positive  $\delta T$ . For  $x < x_c + \delta x_c$ , the convec-  
95 tive region precipitation increases by  $\delta P = M_{qp}(dq_c(T)/dT)\delta T F_T M^{-1}$ , while for  $x > x_c$ ,  
96  $\delta P = 0$ . For the region located within the anomalous shift zone,  $x_c + \delta x_c < x < x_c$ ,  
97 anomalous displacement of the convective margin completely shuts down the mean pre-  
98 cipitation. Thus, the inflow margin shift produces strong droughts in those regions near  
99 the edge of the convective zone that no longer support convection.

100 The convective margin is modeled here as a discontinuity. On timescales of individual  
101 convective events, a sharp convective margin is not unreasonable. However, for longer  
102 timescales (such as monthly averages), the edge of convection tapers smoothly, so that  
103 identification of a distinct convective margin is challenging. Equation (3) provides insight  
104 into smooth edge of the convective zone. For example, consider a wind field consisting  
105 of a steady component  $\bar{u}_q$  and a time-varying, Gaussian perturbation  $\delta u_q$ . Then,  $x_c =$   
106  $\bar{x}_c(1 + \delta u_q \bar{u}_q^{-1}) = \bar{x}_c + \delta x_c$ . Keeping all other parameters fixed, the spatial variation of  $P$   
107 associated with an ensemble of such perturbations is

$$P(x) = \frac{P_0}{2\sigma_{\delta x_c} \sqrt{\pi}} \int_{x-\bar{x}_c}^{\infty} e^{\frac{-\delta x_c^2}{2\sigma_{\delta x_c}^2}} d(\delta x_c) \quad (5)$$

108  $P(x)$  transitions between  $P_0$  and 0 over a characteristic width  $2\sqrt{2}\sigma_{\delta x_c} |\bar{x}_c/\bar{u}_q|$  centered  
 109 on  $\bar{x}_c$ , so wind field transients smooth the convective margin (Figure 2a). Perturbations  
 110 to these more realistic profiles occur on the scale of the mean displacement of  $x_c$  (Figure  
 111 2b).

### 3. Convective margin shifts in El Niño simulations

112 To illustrate the utility of the margins prototype, we consider the impact of El Niño on  
 113 the location of the convective margin, with a regional focus on equatorial South America.  
 114 Our emphasis on this region follows from the substantial El Niño-related precipitation  
 115 anomalies that occur there in both the observations and simulations [e.g., *Hastenrath et*  
 116 *al.*, 1987; *Joseph and Nigam*, 2005]. Mean-state easterly advection of moisture ( $u_q < 0$ )  
 117 is significant in this region because of near-equatorial trade-wind convergence.

118 We compare  $x_c$  predicted by (3) to estimates of the convective margin location derived  
 119 from a 10-member ensemble of 51-year integrations of the Quasi-equilibrium Tropical  
 120 Circulation Model 1 version 2.3 [QTCM1; *Neelin and Zeng*, 2000; *Zeng et al.*, 2000].  
 121 Each ensemble member was initialized from a set of independent initial conditions and  
 122 integrated over the period 1950-2000, with observed sea surface temperatures (SSTs)  
 123 specified over the tropical Pacific and a passive, thermal ocean mixed layer of 50 m depth  
 124 applied elsewhere. Over tropical South America, the mean precipitation increases (at  
 125 least in certain seasons) away from the Atlantic coast to a maximum within the interior  
 126 of the continent. Estimates of the simulated convective margin were obtained by first

127 determining the longitude, relative to the Atlantic coastline, at which the precipitation  
128 field equals half of its maximum climatological value over South America at each latitude,  
129 and then averaging over  $10^{\circ}\text{S}$ - $0^{\circ}$ .

130 For September-October-November (SON), the mean estimated position of the convec-  
131 tive margin as defined here is  $\sim 930$  km from the Atlantic coastline of South America.  
132 Comparison of the margin estimates to NINO3, an index of ENSO variability consisting  
133 of SSTs averaged over  $150^{\circ}\text{W}$ - $90^{\circ}\text{W}$  and  $5^{\circ}\text{S}$ - $5^{\circ}\text{N}$ , indicates that the convective margin  
134 retreats further away from the coast when NINO3 region SSTs are anomalously warm  
135 (Figure 3, triangles). That is, El Niño conditions are associated with a broader noncon-  
136 vecting region, and thus drier-than-normal conditions, over eastern tropical South Amer-  
137 ica. Progressive westward shifting of the convective margin may explain the increase in  
138 the areal extent of tropical droughts with increasing El Niño strength [*Lyon, 2004; Lyon*  
139 *and Barnston, 2005*].

140 The  $x_c$  values predicted by the margin prototype match the estimates derived from  
141 the QTCM1 simulations rather well (Figure 3, squares). Using (3), one can further de-  
142 compose the impact of ENSO forcing on the convective margin by considering how each  
143 factor responds to the forcing. For the ensemble-averaged QTCM1 results, the westward  
144 displacements of  $x_c$  with above normal NINO3 SSTs are principally dominated by the  
145 increase to the convective threshold  $q_c(T)$  as the troposphere warms. Of course,  $\bar{u}_q$  also  
146 becomes more negative (i.e., more easterly) under El Niño conditions and thus enhances  
147 the westward displacement of  $x_c$  over South America. On the other hand,  $q_0$  tends to  
148 increase with positive NINO3 index (since the adjacent tropical Atlantic warms), thereby

149 partially offsetting the westward shifts associated with larger  $q_c(T)$  and anomalous east-  
150 erlies. It should be noted that the relationship between NINO3 and convective margin  
151 location holds for individual ensemble members, although there is greater scatter associ-  
152 ated with atmospheric interval variability.

#### 4. Applicability to the observations

153 A crucial step in assessing the applicability of the margin prototype to the observations  
154 is the identification of circumstances under which the basic assumptions hold. Although  
155 we anticipate that the physics should apply more generally, the simple 1D prototype  
156 developed here can be applied only when the geometries of both the low-level wind and  
157 precipitation fields are relatively uncomplicated. As suggested by the observed Climate  
158 Anomaly Monitoring System (CAMS) rain gauge-derived precipitation [*Chen et al.*, 2002]  
159 and NCAR/NCEP 40-year Reanalysis 850 mb windfield [*Kalnay et al.*, 1996] over tropical  
160 South America, the SON season appears well suited to use of the prototype, since mean  
161 low-level circulation is essentially zonal and normal to the mean precipitation isolines  
162 (Figure 4a; see also the supplementary material). Other caveats, such as fairly constant  
163 inflow moisture values along the coastal margin, are largely satisfied in this season as well.

164 Compositing the SON CAMS rainfall with respect to the El Niño and La Niña phases  
165 of the SON-averaged NINO3 index shows behavior resembling the QTCM1 response to  
166 ENSO. In particular, under El Niño conditions, there is a general westward displacement  
167 of the precipitation isolines over much of near-equatorial South America (red contours).  
168 Consider, for example, the 4 mm day<sup>-1</sup> contour, which generally parallels the Atlantic

169 coastline of South America over  $20^{\circ}\text{S}$ - $10^{\circ}\text{N}$ : the zonal position of this contour under El  
170 Niño conditions is shifted west of its mean location by up to  $5^{\circ}$ .

171 To obtain a more quantitative picture of the changes to the structure of the precipitation  
172 field under El Niño and La Niña conditions, we averaged the composites over  $3.8^{\circ}\text{S}$ -  
173  $1.2^{\circ}\text{S}$ ; results of this averaging appear in Figure 4b. The most pronounced differences  
174 between the El Niño (red line) and La Niña (blue line) longitudinal profiles occur between  
175  $50^{\circ}\text{W}$ - $60^{\circ}\text{W}$ , i.e., at mean precipitation values roughly  $1/3$  to  $1/2$  the peak SON rainfall  
176 values. Relatively small differences prevail where the precipitation rates are highest.  
177 These characteristics are broadly consistent with those shown schematically in Figure 2,  
178 indicating that the notion of viewing the observed precipitation changes in this region as  
179 a convective margin shift has some merit. An assessment of the factors contributing to  
180 the observed margin displacements will be undertaken in future work.

## 5. Summary and discussion

181 We present an analytic prototype of land region convective margins for the case of mois-  
182 ture inflow from a neighboring ocean region. A simple functional expression is obtained  
183 for the position of the convective margin. This expression facilitates diagnosis of pre-  
184 cipitation changes occurring along tropical land region convective margins under climate  
185 perturbation forcing scenarios. For example, comparisons of the simple analytic results to  
186 simulations of ENSO-related precipitation impacts over tropical South America demon-  
187 strate reasonable agreement. Observed precipitation anomalies under certain conditions  
188 also appear consistent with the margin prototype.

189 The convective inflow margin prototype succinctly illustrates (1) the utility of viewing  
190 certain regional precipitation anomalies as shifts in the position of the convective margin;  
191 and (2) the factors affecting such shifts over tropical land regions, including the depen-  
192 dence of the convective threshold on tropospheric temperature and the inflow wind and  
193 moisture values. Although we emphasize here a specific regional impact of El Niño forcing,  
194 the approach is applicable to other tropical land regions as well as other forcing scenarios.  
195 For example, we hope to use the convective margins theory as a template for analyz-  
196 ing regional changes occurring under greenhouse gas warming scenarios as simulated by  
197 different models.

198 **Acknowledgments.** Financial support for this work was provided by NOAA grants  
199 NA04OAR4310013 and NA05OAR4310007 and NFS grant ATM-0082529. BRL also ac-  
200 knowledges partial support of NOAA grant NA03OAR4310066 (John C.H. Chiang, UC  
201 Berkeley)

## References

- 202 Bretherton, C. S., and A. H. Sobel, A simple model of a convectively-coupled Walker  
203 circulation using the weak temperature gradient approximation. *J. Clim.* **15**, 2907–  
204 2920, 2002.
- 205 Chen, M., P. P. Xie, J. E. Janowiak, and P. A. Arkin, Global land precipitation: a 50-year  
206 monthly analysis based on gauge observations. *J. Hydrometeor.* **3**, 249–266, 2002.
- 207 Chiang, J. C. H., and B. R. Lintner, Mechanisms of remote tropical surface warming  
208 during El Niño. *J. Clim.* **18**, 4130–4149, 2005.

209 Chiang, J. C. H., and A. H. Sobel, Tropical tropospheric temperature variations caused  
210 by ENSO and their influence on the remote tropical climate. *J. Clim.* **15**, 2616–2631,  
211 2002.

212 Chou, C., and J. D. Neelin, Mechanisms limiting the northward extent of the northern  
213 summer monsoons over North America, Asia, and Africa. *J. Clim.* **16**, 406–425, 2003.

214 Chou, C., and J. D. Neelin, Mechanisms of global warming impacts on regional tropical  
215 precipitation. *J. Clim.* **17**, 2688–2701, 2004.

216 Dai, A., and T. M. L. Wigley, Global patterns of ENSO-induced precipitation. *Geophys.*  
217 *Res. Let.* **27**, 1283–1286, 2000.

218 Hastenrath, S. L. C. De Castro, and P. Aceituno, The Southern Oscillation in the tropical  
219 Atlantic sector. *Beitr. Phys. Atmos.* **60**, 447–463, 1987.

220 Joseph, R., and S. Nigam, ENSO evolution and teleconnections in IPCC’s 20th century  
221 climate simulations: realistic representation? *J. Clim.* **accepted**, 2005.

222 Kalnay, E., *et al.*, The NCEP/NCAR 40-Year Reanalysis Project, *Bul. Amer. Met. Soc.*  
223 **77**, 437–471, 1996.

224 Klein, S. A., B. J. Soden, and N. C. Lau, Remote sea surface temperature variations  
225 during ENSO: Evidence for a tropical atmospheric bridge. *J. Clim.* **12**, 917–932, 1999.

226 Lintner, B. R., and J. C. H. Chiang, Reorganization of tropical climate during El Niño:  
227 a weak temperature gradient approach. *J. Clim.* **18**, 5312–5329, 2005.

228 Lyon, B., The strength of El Niño and the spatial extent of tropical drought. *Geophys.*  
229 *Res. Let.* **31**, L21204, doi:10.1029/2004GL020901, 2004.

230 Lyon, B., and A. G. Barnston, ENSO and the spatial extent of interannual precipitation  
231 extremes in tropical land areas. *J. Clim.* **18**, 5095–5109, 2005.

232 Neelin, J. D., C. Chou, and H. Su, Tropical drought regions in global warming and El  
233 Niño teleconnections. *Geophys. Res. Lett.* **30**, 2275, doi:10.1029/2003GLO018625, 2003.

234 Neelin, J. D., M. Munnich, H. Su, J. E. Meyerson, and C. E. Holloway, Tropical drying  
235 trends in global warming models and observations. *Proc. Nat. Acad. Sci.* **103**, 6110–6115,  
236 2006.

237 Neelin, J. D., and H. Su, Moist teleconnection mechanisms for the tropical South American  
238 and Atlantic sector. *J. Clim.* **18**, 3928–3950, 2005.

239 Neelin, J. D., and N. Zeng, A quasi-equilibrium tropical circulation model– Formulation.  
240 *J. Atmos. Sci.* **57**, 1741–1766, 2000.

241 Ropelewski, C. F. and M. S. Halpert, Global and regional scale precipitation patterns  
242 associated with the El Niño Southern Oscillation. *Mon. Wea. Rev.* **115**, 1606–1625,  
243 1987.

244 Saravanan, R. and P. Chang, Interaction between tropical Atlantic variability and El Niño  
245 Southern Oscillation. *J. Clim.* **13**, 2177–2194, 2000.

246 Sobel, A. H., I. M. Held, and C. S. Bretherton, The ENSO signal in tropical tropospheric  
247 temperature. *J. Clim.* **15**, 2702–2706, 2002.

248 Su, H. and J. D. Neelin, Teleconnection mechanisms for tropical Pacific descent anomalies  
249 during El Niño, *J. Atmos. Sci.* **59**, 2694–2712, 2002.

250 Wallace, J. M., E. M. Rasmusson, T. P. Mitchell, V. E. Kousky, E. S. Sarachik, and H. von  
251 Storch, The structure and evolution of ENSO-related climate variability in the tropical

252 Pacific: Lesson from TOGA. *J. Geophys. Res. Oceans* **103**, 14241–14259, 1998.

253 Yu, J.-Y., C. Chou, and J. D. Neelin, Estimating the gross moist stability of the tropical  
254 atmosphere. *J. Atmos. Sci.* **55**, 1354–1372.

255 Zeng, N., J. D. Neelin, and C. Chou, A quasi-equilibrium tropical circulation model—  
256 implementation and simulation. *J. Atmos. Sci.* **57**, 1767–1796, 2000.

## 6. Figure Captions

257 **Figure 1:** Schematic overview of the convective margins analysis. Here,  $x_c$  denotes the  
258 position of the convective margin as defined by equation (3), relative to the coast, with  
259 inflow from the ocean.

260 **Figure 2:** Perturbations to the convective margin. (a) illustrates idealized examples of  
261 convective margins subject to stochastic perturbations (equation 5). The profiles reflect  
262 peak precipitation values of 10 and 11 mm day<sup>-1</sup> and margin locations (relative to the  
263 coast) of 925 km and 1075 km; the profile with the higher peak precipitation rate and  
264 greater margin distance from the coast corresponds to a 1K temperature perturbation  
265 relative to the lower precipitation rate/smaller margin location profile. Included in both  
266 profiles is a stochastic perturbation of 2 m s<sup>-1</sup>, or 1/2 the mean  $\bar{u}_q$  (b) shows the difference  
267 between the two Gaussian-perturbed profiles in (a) (solid line); also shown is the difference  
268 for margins without stochastic effects (dashed line).

269 **Figure 3:** Convective margin position variations over equatorial South America from  
270 QTCM1 simulations. Simulated margin locations (x-axis; in km) were estimated from the  
271 longitude at which the total precipitation, averaged over September-October-November  
272 (SON) and 10°S-0°, achieved half its maximum climatological value in the interval 70°W-  
273 30°W. The longitude values were converted to distances relative to the mean South Amer-  
274 ican Atlantic coastal margin longitude (41°W) between 10°S-0°S. Plotted against these  
275 estimates are values of the NINO3 index (in K; triangles) as well as margin prototype  $x_c$   
276 predicted by equation (3) (in km; squares).

277 **Figure 4:** SON composites of observed CAMS rain gauge precipitation for South  
278 America during 1950-2000. In (a), the El Niño phase average (red contours) consists of  
279 those years for which the SON-averaged NINO3  $\geq 1$  standard deviation, while the La Niña  
280 phase (blue contours) consists of those years with NINO3  $\leq -1$  standard deviation. Also  
281 shown are the mean SON precipitation over all years (black contours, shaded for emphasis)  
282 and the mean 850 mb windfield (vectors) from the NCAR/NCEP 40-year Reanalysis.  
283 Panel (b) illustrates longitudinal transects, averaged over the stippled area in (a), for El  
284 Niño (red), La Niña (blue), and all (black) years.

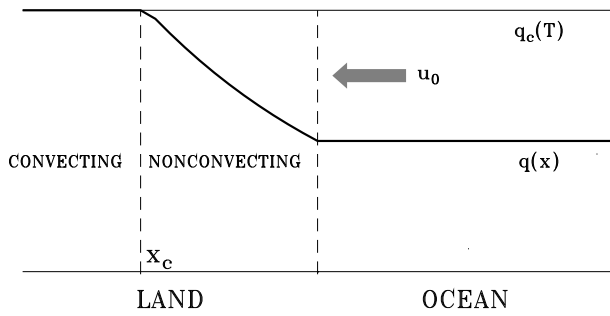


**Figure 1.** Schematic overview of the convective margins analysis. Here,  $x_c$  denotes the position of the convective margin as defined by equation (3), relative to the coast, with inflow from the ocean.

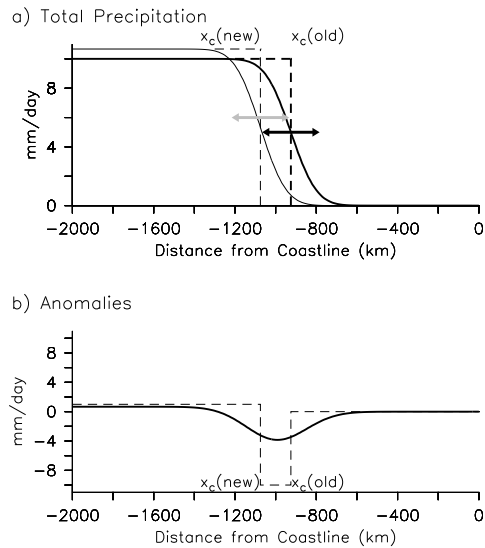


**Figure 2.** Perturbations to the convective margin. (a) illustrates idealized examples of convective margins subject to stochastic perturbations (equation 5). The profiles reflect peak precipitation values of 10 and 11 mm day<sup>-1</sup> and margin locations (relative to the coast) of 925 km and 1075 km; the profile with the higher peak precipitation rate and greater margin distance from the coast corresponds to a 1K temperature perturbation relative to the lower precipitation rate/smaller margin location profile. Included in both profiles is a stochastic perturbation of 2 m s<sup>-1</sup>, or 1/2 the mean  $\bar{u}_q$  (b) shows the difference between the two Gaussian-perturbed profiles in (a) (solid line); also shown is the difference for margins without stochastic effects (dashed line).

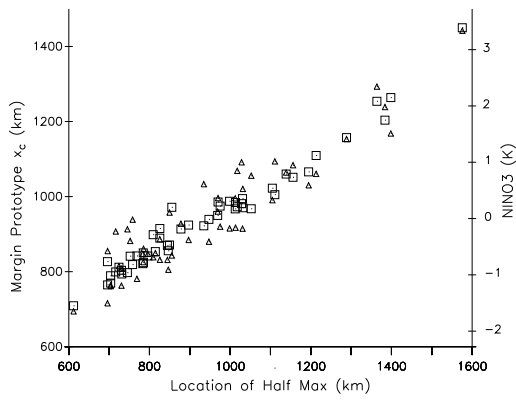


**Figure 3.** Convective margin position variations over equatorial South America from QTCM1 simulations. Simulated margin locations (x-axis; in km) were estimated from the longitude at which the total precipitation, averaged over September-October-November (SON) and  $10^{\circ}\text{S}$ - $0^{\circ}$ , achieved half its maximum climatological value in the interval  $70^{\circ}\text{W}$ - $30^{\circ}\text{W}$ . The longitude values were converted to distances relative to the mean South American Atlantic coastal margin longitude ( $41^{\circ}\text{W}$ ) between  $10^{\circ}\text{S}$ - $0^{\circ}\text{S}$ . Plotted against these estimates are values of the NINO3 index (in K; triangles) as well as margin prototype  $x_c$  predicted by equation (3) (in km; squares).

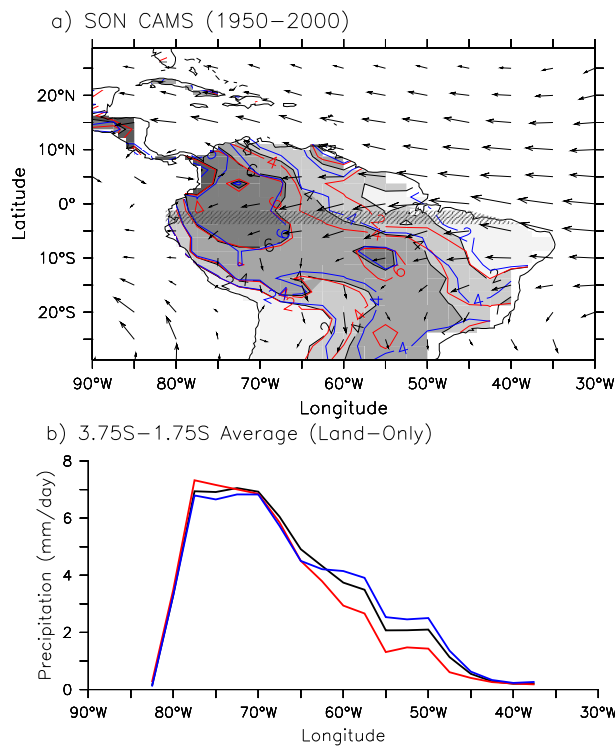


**Figure 4.** SON composites of observed CAMS rain gauge precipitation for South America during 1950-2000. In (a), the El Niño phase average (red contours) consists of those years for which the SON-averaged NINO3  $\geq 1$  standard deviation, while the La Niña phase (blue contours) consists of those years with NINO3  $\leq -1$  standard deviation. Also shown are the mean SON precipitation over all years (black contours, shaded for emphasis) and the mean 850 mb windfield (vectors) from the NCAR/NCEP 40-year Reanalysis. Panel (b) illustrates longitudinal transects, averaged over the stippled area in (a), for El Niño (red), La Niña (blue), and all (black) years.